



Cite this: *Nanoscale*, 2017, **9**, 9284

Received 16th March 2017,

Accepted 7th June 2017

DOI: 10.1039/c7nr01860f

rsc.li/nanoscale

## Ultra-high sensitivity infra-red detection and temperature effects in a graphene–tellurium nanowire binary hybrid†

Avradip Pradhan,<sup>a</sup> Ahin Roy,<sup>a</sup> Shalini Tripathi,<sup>b</sup> Anirban Som,<sup>c</sup> Depanjan Sarkar,<sup>c</sup> Jayanta Kumar Mishra,<sup>a</sup> Kallol Roy,<sup>a</sup> T. Pradeep,<sup>c</sup> N. Ravishankar<sup>b</sup> and Arindam Ghosh<sup>a,d</sup>

The optoelectronic performance of hybrid devices from graphene and optically sensitive semiconductors exceeds conventional photodetectors due to a large in-built optical gain. Tellurium nanowire (TeNW), being a narrow direct band gap semiconductor (~0.65 eV), is as an excellent potential candidate for near infra-red (NIR) detection. Here we demonstrate a new graphene–TeNW binary hybrid that exhibits a maximum photoresponsivity of ~10<sup>6</sup> A W<sup>-1</sup> at 175 K in the NIR regime (920 nm–1720 nm), which exceeds the photoresponsivity of the most common NIR photodetectors. The resulting noise-equivalent power (NEP) is as low as 2 × 10<sup>-18</sup> W Hz<sup>-1/2</sup>, and the specific detectivity (D\*) exceeds 5 × 10<sup>13</sup> cm Hz<sup>1/2</sup> W<sup>-1</sup> (Jones). The temperature range of optimal operation, which extends up to ~220 K and ~260 K for 1720 nm and 920 nm excitation, respectively, is primarily limited by the electrical conductivity of the TeNW layer, and can further be improved by lowering of the defect density as well as inter-wire electronic coupling.

Infra-red (IR) detection has drawn a lot of attention because of its practical applications in various fields, such as satellite and fiber-optic communication, night vision and surveillance, remote sensing and thermal imaging. Most of these IR photodetectors are based on quantum dots and wells,<sup>1–4</sup> carbon nanotubes,<sup>5,6</sup> organic polymers,<sup>7,8</sup> nanocrystals,<sup>9–11</sup> transition metal dichalcogenides (TMDCs)<sup>12,13</sup> and other low band gap semiconductor systems. Two of the major IR detectors are photodiodes and photoconductors, where the latter can exhibit enhanced photoresponsivity  $\gamma$ , which is the ratio of the photo-generated current ( $I_p$ ) to the incident optical

power  $P$ , due to a high optical gain. A large photoresponsivity allows attaining low noise-equivalent power,  $NEP = \sqrt{(2eI_d + 4k_B T/R)}/\gamma$ , (where  $I_d$  is the dark state current,  $T$  is the temperature and  $R$  is the resistance of the channel) and large specific detectivity,  $D^* = \sqrt{A}/NEP$  ( $A$  is the detector active area). Among the room temperature IR-detectors, the highest specific detectivity is reported from solution cast PbS quantum dots ( $D^* \approx 1.8 \times 10^{13}$  cm Hz<sup>1/2</sup> W<sup>-1</sup> or Jones at 1300 nm).<sup>1</sup> InAs/InGaAs-based low band gap semiconductor heterostructures and self-assembled quantum dot devices exhibit exceptionally low NEP (10<sup>-18</sup>–10<sup>-19</sup> W Hz<sup>-1/2</sup>), making these devices suitable for single photon detection in the telecommunication range (~1550 nm).<sup>14–16</sup> These devices, however, mostly operate at liquid helium temperatures ( $\lesssim 4$  K), and constructing a high-temperature, low-noise and broadband (~800–2000 nm) NIR detector remains an outstanding technological challenge.

Single layer graphene<sup>17</sup> has traditionally been of great interest for photodetection due to its strong coupling to radiation (coupling coefficient ~10<sup>7</sup> m<sup>-1</sup>) over a broad range of the electromagnetic spectrum (~0.3–6  $\mu$ m). Bare graphene photodetectors are used for broadband photodetection,<sup>18</sup> although the sensitivity of these devices is relatively poor because of low net optical absorption (~2%) by graphene. Alternative designs<sup>19</sup> of graphene photodetectors sensitized with diverse underlying physical mechanisms from metal plasmonic coupling,<sup>20,21</sup> photogating,<sup>22</sup> photothermoelectric<sup>23</sup> and photovoltaic<sup>24</sup> to bolometric<sup>25</sup> have also been demonstrated. Of particular interest are graphene–semiconductor heterojunctions and heterostructures,<sup>22,26–32</sup> where a physical separation of the photogenerated electrons and holes can lead to an extremely long carrier lifetime (up to several seconds), and hence a very high optical gain. This has led not only to large  $\gamma \sim 10^{10}$  A W<sup>-1</sup> in MoS<sub>2</sub>–graphene hybrid devices, but also unexpected optoelectronic effects, such as persistent photoconductivity.<sup>22</sup> In the IR regime, hybrid devices of graphene electrodes sandwiching a Ta<sub>2</sub>O<sub>5</sub> film exhibit room temperature IR photoresponsivity  $\gamma \approx 1$  A W<sup>-1</sup> for photoexcitation wavelengths up to

<sup>a</sup>Department of Physics, Indian Institute of Science, Bangalore 560012, India.  
 E-mail: avradip@physics.iisc.ernet.in, arindam@physics.iisc.ernet.in

<sup>b</sup>Materials Research Centre, Indian Institute of Science, Bangalore 560012, India

<sup>c</sup>Department of Chemistry, Indian Institute of Technology Madras, Chennai 600036, India

<sup>d</sup>Centre for Nano Science and Engineering, Indian Institute of Science, Bangalore 560012, India

†Electronic supplementary information (ESI) available. See DOI: 10.1039/C7NR01860F

3  $\mu\text{m}$ .<sup>33</sup> IR specific detectivity as high as  $\approx 7 \times 10^{13}$  Jones has been reported when a planar array of PbS quantum dots is self-assembled on the surface of a graphene field effect transistor,<sup>34</sup> where the quantum dot layer serves as an optical gate in the presence of illumination. However, in spite of promising characteristics, the performance of graphene-based NIR phototransistor designs with other partner nanomaterials, and also the effect of temperature, remain largely unexplored.

Here we report the NIR photoresponsivity and specific optical detectivity of graphene–tellurium nanowire (TeNW) binary hybrid devices. Tellurium (Te) is a semiconductor with a trigonal crystal structure having a bulk band gap of  $\sim 0.35$  eV. It is often used as a thermoelectric material, gas sensor, piezoelectric material and also in optoelectronics and other applications.<sup>35–38</sup> In the nanowires of diameter ranging between  $\sim 5$ – $10$  nm, the band gap increases to  $\approx 0.65$  eV (see section S2 in the ESI†), making TeNWs excellent candidate for photoabsorption in the NIR regime. A planar ensemble of TeNWs exhibits large in-plane resistance due to their weak inter-wire electronic coupling which allows, when dropcast on the surface of a graphene field-effect transistor (FET), the formation of a photosensitive hybrid, similar to that of graphene and self-assembled quantum dots.<sup>34</sup> Our experiment reveals photoresponsivity  $\gamma$  as large as  $10^6$  A W<sup>-1</sup>, and specific detectivity  $D^* > 10^{13}$  Jones in the hybrid over a broad range of wave-

lengths ( $\sim 920$ – $1720$  nm), exceeding those of the most existing (cooled) NIR photodetectors by over an order of magnitude.<sup>11,12,39–42</sup> Moreover, a systematic temperature-dependence of the photoresponse reveals that the maximum operating temperature ( $\sim 220$ – $260$  K) of these devices is mainly limited by the electrical conductivity of the TeNW layer, which can be further enhanced by lowering the defect density and inter-wire electronic coupling.

In order to fabricate the graphene–TeNW hybrid, single layer graphene was mechanically exfoliated on the standard Si/SiO<sub>2</sub> (285 nm) substrate followed by electron beam lithography for the contact pads, and 5 nm/50 nm of Cr/Au metallization. Finally, TeNWs (suspended in ethanol solution) were dropcast on the graphene FET, and spread uniformly over the device area (see schematic of Fig. 1(a)). More details of the TeNW growth process and dispersion over a pre-determined area of the substrate can be found in sections S1 and S3 of the ESI.† The electrical and optical measurements were carried out using a home-made variable-temperature optical cryostat having four power-calibrated LEDs of different wavelengths (920 nm, 1300 nm, 1550 nm and 1720 nm) mounted on an optical window. The drain–source voltage ( $V_{DS}$ ) is applied across two metal electrodes, and the corresponding drain–source current ( $I_{DS}$ ) is monitored using a lock-in amplifier. Fig. 1(b) shows the SEM image of a representative graphene–

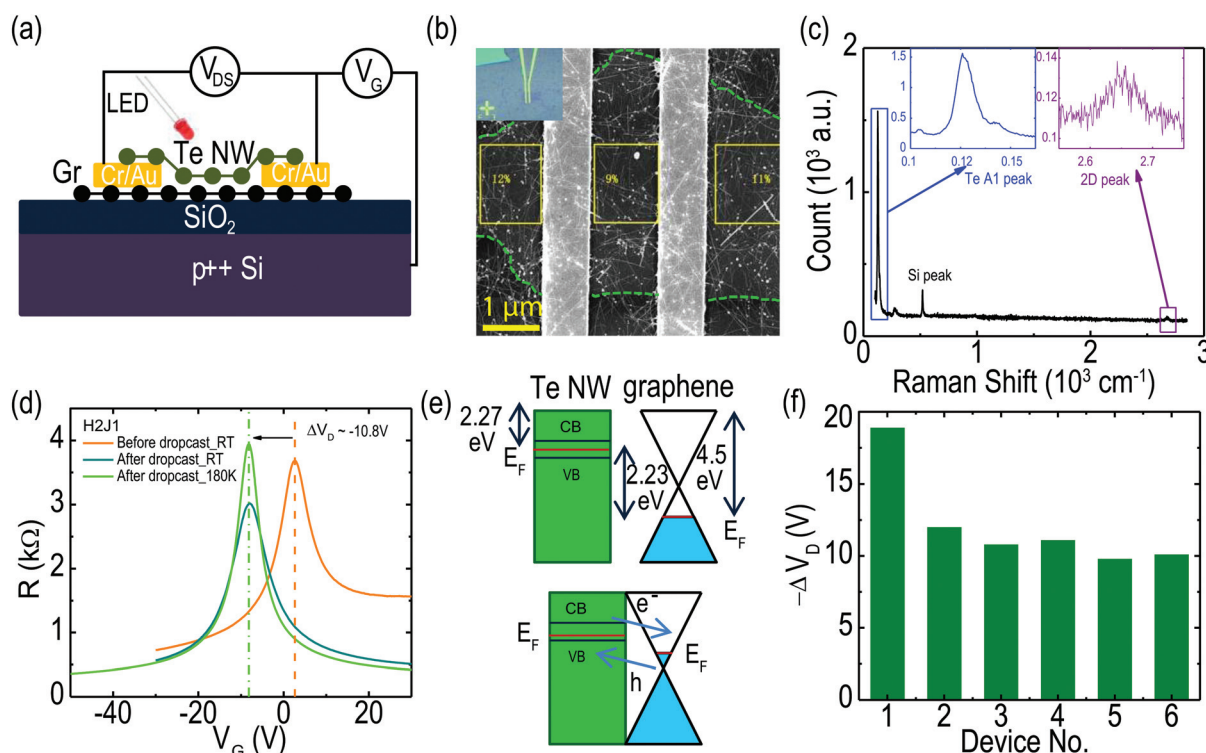


**Fig. 1** Device structure and characteristics: (a) Schematic of the graphene–TeNW hybrid along with the circuit diagram for optoelectronic measurements. (b) SEM image of a representative graphene–TeNW binary hybrid. The graphene area has been outlined with a green dashed line. The area fraction coverage of TeNWs on graphene is calculated directly (see Fig. S4 in the ESI† for further details) and mentioned in the image box. The inset shows the optical image of the same device. (c) Raman spectroscopy of the hybrid showing the spectra of both Te (A<sub>1</sub> peak) and graphene (2D peak). (d) Transfer characteristics ( $R$ – $V_G$ ) of the graphene–TeNW hybrid device before and after the dropcast of TeNWs. (e) Band diagram schematic showing the initial electron doping of graphene from TeNWs. (f) Histogram of the shift in the Dirac point ( $\Delta V_D$ ) for all measured devices.

TeNW device, with a typical channel length of  $\sim 1.5\text{--}2\ \mu\text{m}$ . The inset also shows the optical image of the same device. Importantly, due to limited control on the dropcast process, the layer of TeNWs extends onto both metal electrodes, thereby making a parallel transport channel with graphene. However, the in-plane resistance of the layer at a low temperature ( $T \sim 175\ \text{K}$ ) exceeds  $1\ \text{M}\Omega$  (see Fig. 4(d)), considerably larger than the typical graphene channel resistance ( $\sim 2\text{--}10\ \text{k}\Omega$ ). Therefore, the conduction through the TeNW layer can be neglected, particularly at  $T \lesssim 200\ \text{K}$ . Structural characterization using Raman spectroscopy shows the high crystallinity of both the members in the hybrid (Fig. 1(c), also see section S4 as well as Fig. S2(c) in the ESI† for HRTEM images of individual TeNWs). The inset shows the typical Raman active  $A_1$  mode peak for Te ( $\sim 125\ \text{cm}^{-1}$ ),<sup>44</sup> and the 2D peak for graphene,<sup>45</sup> whose strength is weakened due to the presence of intervening TeNW layer.

The electrical characteristics of the hybrid are shown in Fig. 1(d). The orange and blue traces represent room temperature dark-state transfer characteristics (resistance-gate voltage:  $R\text{--}V_G$ ) of the device before and after the dropcast of the TeNW layer respectively. The light green trace shows the post-dropcast characteristics at  $T = 180\ \text{K}$ . The shift in the charge neutrality point (Dirac point) towards the negative side of the gate voltage

after the dropcast ( $\Delta V_D \sim -10.8\ \text{V}$  in this case) suggests electron doping in the graphene channel. This can be easily understood from the band alignment in TeNWs and graphene when the hybrid is formed (Fig. 1(e)). The difference between the workfunction of graphene ( $\sim 4.5\ \text{eV}$ ), and the electron affinity of TeNWs ( $\sim 1.97\ \text{eV}$ ) in the presence of a band gap of  $\approx 0.65\ \text{eV}$ , places the Fermi level of the TeNWs about  $\sim 2.2\ \text{eV}$  above that of undoped graphene. The resulting flow of charge leads to intrinsic electron doping of the graphene channel, as confirmed in Fig. 1(d). The consistency of the shift magnitude, with  $\Delta V_D \sim -10\ \text{V}$  in over 80% devices (Fig. 1(f)), confirms the device or processing-independent transparency of the interface to charge transfer, which is crucial for the charge separation and the photogating effect during optical illumination.

The optoelectronic response of the hybrid, illustrated for the excitation wavelength  $920\ \text{nm}$  at an optical power level of  $7741.0\ \text{fW}\ \mu\text{m}^{-2}$  ( $T = 175\ \text{K}$ ), is shown in Fig. 2. The experiment involves recording the change in the device resistance across periodic cycles of switching on and turning off of the optical illumination. Two such cycles at five different values of  $V_G$  across the Dirac point are shown in Fig. 2(a). It is evident that both the sign and magnitude of the photoresponse vary with  $V_G$ , and the latter is reversed on the opposite sides of the Dirac point. On the negative side of the Dirac point, when graphene

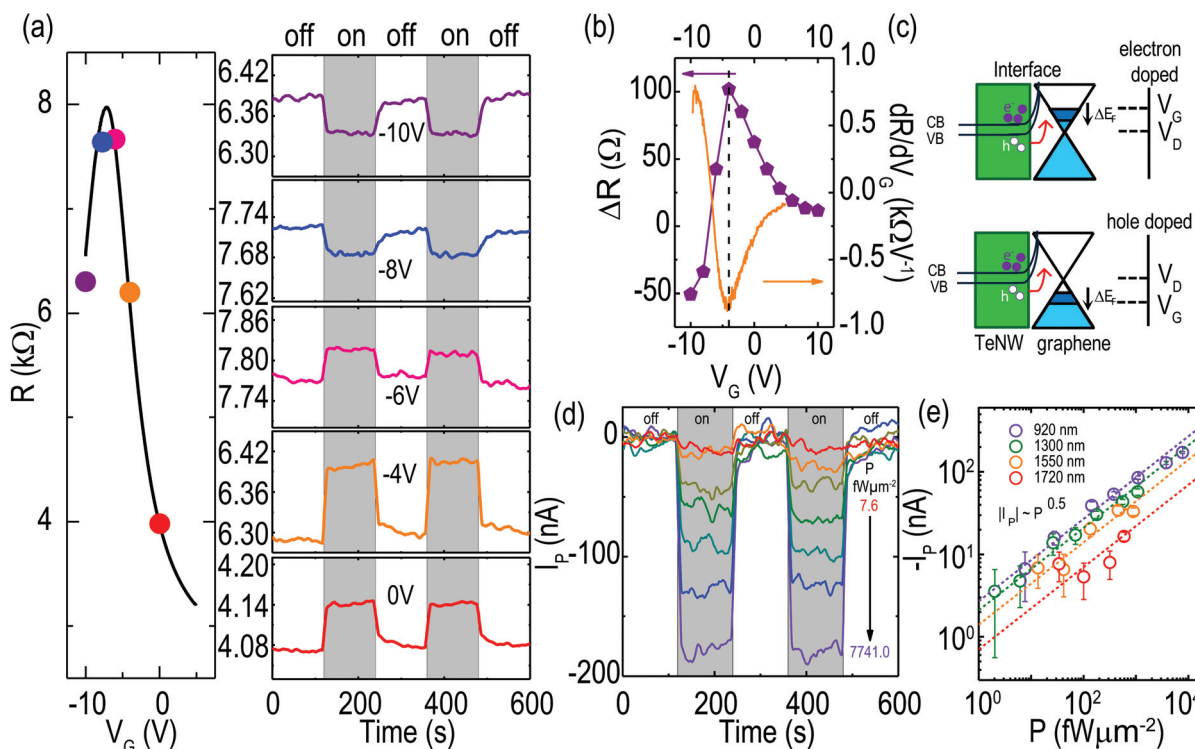


**Fig. 2** Transfer characteristics and photoresponse in the infra-red regime: (a) Transfer characteristics ( $R\text{--}V_G$ ) and photoresponse with light on-off cycles at five different gate voltages. Note the change in the sign of the photoresponse as the gate voltage is swept through the Dirac point. (b) Gate voltage dependence of the photoresponse ( $\Delta R$ ). The coincidence of the maxima with that of the derivative of the  $R\text{--}V_G$  shows the photogating effect. (c) Schematic of charge transfer and the photogating effect on both electron doped and hole doped regimes. (d) Time dependence of the photocurrent ( $I_p$ ) at different photoexcitation (LED) powers (7.6, 27.7, 143.9, 379.5, 1079.2, 3776.7 and 7741.0  $\text{fW}\ \mu\text{m}^{-2}$ ) in the light on-off experiment (excitation wavelength =  $920\ \text{nm}$  at  $V_G = -2\ \text{V}$ ). (e) Photocurrent ( $I_p$ ) as a function of photoexcitation power  $P$  for all the 4 wavelengths. The dotted lines indicate  $I_p \propto P^{0.5}$ .

is hole-doped, the photoresponse is positive, *i.e.* the resistance decreases on photoillumination, whereas the resistance increases on photoillumination when graphene is electron doped (positive side of the Dirac point). The variation in  $\Delta R = R_{\text{on}} - R_{\text{off}}$  over the entire range of  $V_G$  is plotted in Fig. 2(b), which shows a maximum change in the resistance of  $\sim 100\%$  ( $\approx 2\%$ ), and reverses the sign at the Dirac point ( $\approx -7$  V).

The photoresponse in the graphene–TeNW hybrids can be readily explained by the photogating effect, which involves physical separation of the photogenerated electrons and holes by transfer of one of the charges to the graphene layer immediately upon formation. This charges up the absorber layer with charge a density  $\sigma \sim \eta\tau(P\lambda/hc)$  in the presence of optical excitation, where  $\eta$ ,  $\tau$ ,  $P$  and  $\lambda$  are the quantum efficiency, lifetime of photogenerated electron–hole pairs, optical power and wavelength of the excitation, respectively. The resulting shift in the gate voltage manifests in the change in resistance,  $\Delta R = (dR/dV_G)(d_{\text{int}}\sigma/\epsilon_0\epsilon_r)$ , where  $d_{\text{int}}$  is equivalent to the depletion length scale at the graphene–TeNW interface. The observation  $\Delta R \propto -dR/dV_G$  (see Fig. 2(b)) establishes the photogating effect in our case. Moreover, the negative proportionality also implies that the TeNW layer is negatively charged, with the transferring of holes to graphene.

The microscopic mechanism driving charge transfer can be explained by the schematic shown in Fig. 2(c). During the formation of the hybrid, electrons flow from TeNWs towards gra-

phene due to the interfacial potential drop (Fig. 1(e)), and bend the bands upward in order to prevent the electron flow indefinitely. Once the electron and hole pairs are generated by optical illumination, this interfacial barrier will readily allow the holes to crossover to graphene while retaining the electrons in the TeNW layer, making it negatively charged. This naturally explains the negative and positive signs of  $\Delta R$  in the hole and electron doped regimes, respectively.

Fig. 2(d) illustrates the variation in the photoresponse, in terms of photocurrent  $I_P = -V_{\text{DS}}\Delta R/R^2$ , as the photoexcitation power is increased.  $I_P$  increases sublinearly with  $P$  (Fig. 2(e)) with an exponent  $\sim 0.5$ . Intriguingly, it can be noted from the time cycles shown in Fig. 2(d) that, unlike graphene–MoS<sub>2</sub><sup>46</sup> or graphene–PbS quantum dot<sup>34</sup> hybrids, the relaxation in  $I_P$  on switching the illumination on or off is exceptionally fast, limited essentially by the speed of our measurement  $\sim 300$  ms (see section S5 in the ESI† for more details). Apart from suggesting a trap-free graphene–TeNW interface, this observation may also facilitate the construction of high speed IR detectors, although the precise detection speed will require further experimentation.

Fig. 3 summarizes the optoelectronic performance of the graphene–TeNW hybrid device. Fig. 3(a) shows the photoresponsivity  $\gamma = I_P/(PA)$ , ( $A = LW$ ,  $L$  and  $W$  being the length and width of the graphene channel respectively) as a function of illumination power density. For all wavelengths,  $\gamma$  is enhanced

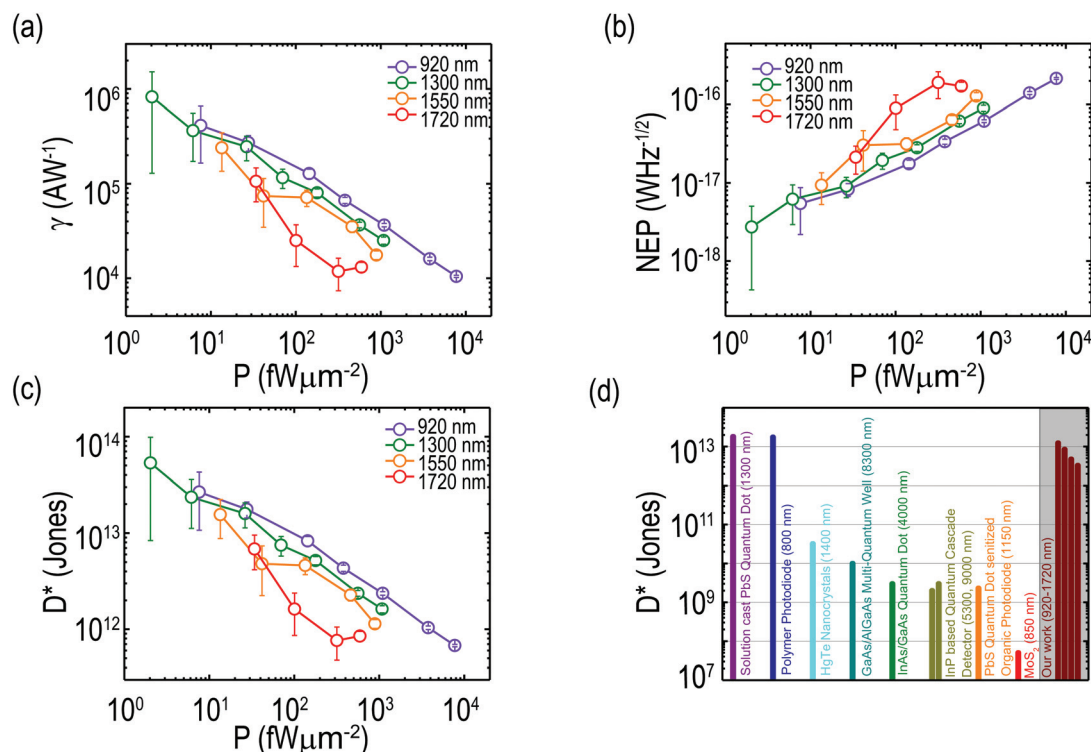


**Fig. 3** Photoresponse figure of merit of the graphene–TeNW hybrid at 175 K: (a) Photoresponsivity ( $\gamma$ ) for different photoexcitation wavelengths in the IR regime. The maximum  $\gamma$  observed is as high as  $10^6$  A W<sup>-1</sup>. (b) Noise-equivalent power (NEP) as a function of  $P$ . (c) Specific detectivity ( $D^*$ ) as a function of  $P$  for the same range of photoexcitation wavelengths. (d) Comparison of the specific detectivity ( $D^*$ ) using different IR detectors.<sup>1,11,12,39–43</sup> The shaded regime includes the results of our work with  $P = 60$  fW  $\mu\text{m}^{-2}$ .

as  $P$  decreases. This has been observed previously, and has been explained in terms of space charge generation and reduction of the quantum efficiency of the device at high power.<sup>22,34,47,48</sup> This will limit the linear dynamic range to  $P \lesssim 50 \text{ fW } \mu\text{m}^{-2}$  (for wavelengths  $\lambda < 1550 \text{ nm}$ ). Importantly, the maximum  $\gamma$  can be as high as  $\sim 10^6 \text{ A W}^{-1}$ , and seems to depend weakly on the excitation wavelength for most values of  $P$  in our experimental range. Remarkably, the high responsivity could be achieved in spite of just  $\sim 10\%$  area coverage by the nanowires which is significantly smaller than the coverage in graphene–quantum dot hybrids,<sup>34</sup> presumably due to an enhanced contact area and hence the number of charge transfer channels. The  $P$ -dependence of  $NEP$  and  $D^*$  for the same wavelengths is shown in Fig. 3(b) and (c), respectively. While  $NEP$  approaches the resolution of  $\sim 10$ – $100$  photons within a bandwidth of  $\sim 1 \text{ Hz}$ , the specific detectivity can be as large as  $6 \times 10^{13}$  Jones at low power levels. A comparison of the specific detectivity ( $D^*$ ) of the graphene–TeNW hybrid with some of the known high-sensitivity IR detectors is also compiled in Fig. 3(d).

The lifetime of the electron hole pairs ( $\tau$ ) can be estimated from the known value of photoresponsivity  $\gamma$ . The external quantum efficiency ( $\eta_{\text{ext}}$ ) is related to  $\gamma$  as  $\eta_{\text{ext}} = \gamma hc / \lambda e$ , which is again related to the internal quantum efficiency ( $\eta_{\text{int}}$ ) as  $\eta_{\text{ext}} = \eta_{\text{int}} G$ , where  $G$  is known as the photoconducting gain. For  $\gamma \approx 10^6 \text{ A W}^{-1}$  and  $\lambda = 920 \text{ nm}$ ,  $\eta_{\text{ext}}$  is estimated to be  $\sim 1.35 \times 10^6$ . From a known value of  $\eta_{\text{int}}$  reported before as  $\sim 0.3$ ,<sup>22</sup>  $G$  is estimated to be  $\approx 4.5 \times 10^6$ . Now, the transit time of the carriers

( $\tau_{\text{transit}}$ ) can be estimated as  $\tau_{\text{transit}} = L^2 / \mu V_{\text{DS}}$ , where  $\mu$  is the mobility of the graphene channel. For  $L \sim 2 \mu\text{m}$ ,  $\mu \sim 0.6 \text{ m}^2 \text{ V}^{-1} \text{ s}^{-1}$  and  $V_{\text{DS}} = 50 \text{ mV}$ ,  $\tau_{\text{transit}}$  comes out to be  $1.33 \times 10^{-10} \text{ s}$ . Finally, the relation  $G = \tau / \tau_{\text{transit}}$  gives  $\tau \approx 5.99 \times 10^{-4} \text{ s}$ , which, as per our expectation, is much longer than  $\tau_{\text{transit}}$  because of the spatial charge separation at the graphene–TeNW interface.

We finally address the variation of photoresponse in our hybrid devices with temperature. Fig. 4(a) shows the dependence of  $\gamma$  for different NIR wavelengths (at fixed  $P = 600 \text{ fW } \mu\text{m}^{-2}$ ) on  $T$  between  $175 \text{ K}$  and  $280 \text{ K}$ . The photocurrent decreases with increasing temperature for all wavelengths.  $\gamma$  becomes immeasurably small at a lower  $T$  ( $\sim 220 \text{ K}$ ) for the longest photoexcitation wavelength ( $1720 \text{ nm}$ ) in our experiment, but survives up to a maximum of  $\approx 260 \text{ K}$  for the shortest wavelength ( $920 \text{ nm}$ ), suggesting that thermal fluctuations are the key factors for the diminishing photoresponse with increasing  $T$ . Indeed, an Arrhenius plot (Fig. 4(b)) of  $\gamma$  vs.  $T^{-1}$  indicates, within the experimental error, an activated behavior of  $\gamma$  with activation energy  $\Delta_P \approx 80 \text{ meV}$ , irrespective of the wavelength.

In order to explore the microscopic origin of this energy scale, we have performed direct transport measurement on a bare TeNW layer (without graphene), which was separately grown on a cover slip (glass) substrate. Following an identical metallization process (Cr/Au:  $5 \text{ nm}/50 \text{ nm}$ ) *via* shadow masking, which defines the effective device length of  $\approx 100 \mu\text{m}$ , the zero bias electrical resistance ( $R_w$ ) was measured

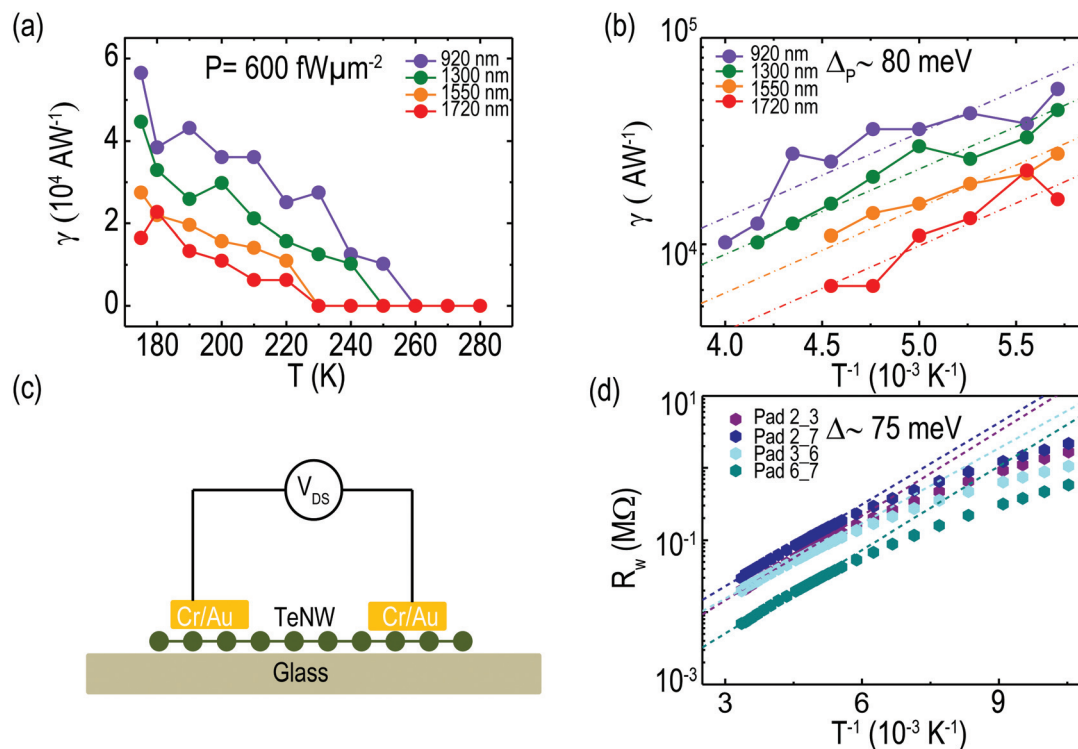


**Fig. 4** Temperature dependence of the photoresponse of the binary hybrid and electrical conductance of TeNWs: (a) Temperature dependence of the photoresponsivity ( $\gamma$ ) for different photoexcitation wavelengths at fixed  $P = 600 \text{ fW } \mu\text{m}^{-2}$ . (b) Arrhenius plot for the photoresponsivity ( $\gamma$ ) of the hybrid device. (c) Schematic of the bare TeNW device on the cover slip substrate along with the circuit diagram for the electrical measurements. (d) Arrhenius plot for the temperature dependence of the resistance of the bare TeNW devices.

using a two-probe technique (see schematic of Fig. 4(c)). Multiple regions from the same planar ensemble of the TeNWs on glass were measured to obtain overall in-plane transport characteristics of the TeNW layer. Fig. 4(d) shows the activated variation of  $R_w$  with  $T$  in four representative areas of the ensemble at a higher  $T$ , which weakens at a lower  $T$ , presumably due to an onset of variable range hopping-like transport. Strikingly, the average activation energy of  $\sim 75$  meV (dashed lines) closely agrees with the activation energy scale  $\Delta_P$  from photoresponsivity measurements (Fig. 4(b)), suggesting that the suppression of  $\gamma$  is closely linked to the electrical conductance of the TeNW layer. This link can be readily understood as leaking of photogenerated charge through the source and drain electrodes because of increasing conductance of the TeNW layer at higher  $T$ . The microscopic origin of  $\Delta_P$  is not fully understood. Since  $\Delta_P \ll$  TeNW band gap ( $\approx 0.65$  eV), this could represent an impurity band transport through the acceptor levels in TeNWs,<sup>49</sup> even though the energy of these levels is larger than the observed  $\Delta_P$ , a renormalization at the nanoscale cannot be ruled out. Alternatively,  $\Delta_P$  could also represent inter-wire hopping transport, which has been shown<sup>50–52</sup> to determine in-plane transport in the ensemble of ultra-thin nanowires. The proximity to the substrate and the nature of the functionalized ligand strongly impact the hopping energy scales,<sup>51,52</sup> which can also be tuned to impede back-transfer of charge from graphene to the TeNWs, thus enhancing the operating temperature of the hybrid.

In summary, we have studied the near infra-red photo-response in a graphene–TeNW binary hybrid over a range of gate voltages and temperatures. These devices exhibit extremely large photoresponsivity and, correspondingly, low noise-equivalent power, in the wavelength range of  $\sim 920$ – $1720$  nm. The resulting specific detectivity exceeds that of the most common (cooled) NIR photodetectors by nearly an order of magnitude. While large area scalability with bulk production of TeNWs<sup>53</sup> and chemical vapour deposition of graphene<sup>22</sup> are clear advantages, the temperature effect on the photoresponse shows a limited operating temperature range, which can be addressed by further interface engineering.

The authors would like to acknowledge the DST (Department of Science and Technology), Govt. of India for financial support. AP, JKM and KR also acknowledge CeNSE (Centre for Nano Science and Engineering, IISc Bangalore) for providing the central facilities e.g. electron beam lithography, Raman spectroscopy, etc.

## References

- G. Konstantatos, I. Howard, A. Fischer, S. Hoogland, J. Clifford, E. Klem, L. Levina and E. H. Sargent, *Nature*, 2006, **442**, 180–183.
- S. A. McDonald, G. Konstantatos, S. Zhang, P. W. Cyr, E. J. Klem, L. Levina and E. H. Sargent, *Nat. Mater.*, 2005, **4**, 138–142.
- C.-Y. Chang, H.-Y. Chang, C.-Y. Chen, M.-W. Tsai, Y.-T. Chang, S.-C. Lee and S.-F. Tang, *Appl. Phys. Lett.*, 2007, **91**, 163107.
- A. Rogalski, J. Antoszewski and L. Faraone, *J. Appl. Phys.*, 2009, **105**, 091101.
- B. Pradhan, K. Setyowati, H. Liu, D. H. Waldeck and J. Chen, *Nano Lett.*, 2008, **8**, 1142–1146.
- P. W. Barone, S. Baik, D. A. Heller and M. S. Strano, *Nat. Mater.*, 2005, **4**, 86–92.
- E. Perzon, F. Zhang, M. Andersson, W. Mammo, O. Inganäs and M. R. Andersson, *Adv. Mater.*, 2007, **19**, 3308–3311.
- P. H. Wöbkenberg, J. G. Labram, J.-M. Swiecicki, K. Parkhomenko, D. Sredojevic, J.-P. Gisselbrecht, D. M. de Leeuw, D. D. Bradley, J.-P. Djukic and T. D. Anthopoulos, *J. Mater. Chem.*, 2010, **20**, 3673–3680.
- T. Aqua, R. Naaman, A. Aharoni, U. Banin and Y. Paltiel, *Appl. Phys. Lett.*, 2008, **92**, 223112.
- G. Konstantatos, L. Levina, J. Tang and E. H. Sargent, *Nano Lett.*, 2008, **8**, 4002–4006.
- M. Böberl, M. V. Kovalenko, S. Gamerith, E. J. List and W. Heiss, *Adv. Mater.*, 2007, **19**, 3574–3578.
- W. Choi, M. Y. Cho, A. Konar, J. H. Lee, G.-B. Cha, S. C. Hong, S. Kim, J. Kim, D. Jena, J. Joo and S. Kim, *Adv. Mater.*, 2012, **24**, 5832–5836.
- K. Zhang, *et al.*, *ACS Nano*, 2016, **10**, 3852–3858.
- M. Ward, O. Karimov, D. Unitt, Z. Yuan, P. See, D. Gevaux, A. Shields, P. Atkinson and D. Ritchie, *Appl. Phys. Lett.*, 2005, **86**, 201111.
- C. Zinoni, B. Alloing, C. Monat, V. Zwiller, L. Li, A. Fiore, L. Lunghi, A. Gerardino, H. De Riedmatten, H. Zbinden and N. Gisin, *Appl. Phys. Lett.*, 2006, **88**, 131102.
- M. T. Rakher, L. Ma, O. Slattery, X. Tang and K. Srinivasan, *Nat. Photonics*, 2010, **4**, 786–791.
- K. S. Novoselov, A. K. Geim, S. V. Morozov, D. Jiang, Y. Zhang, S. V. Dubonos, I. V. Grigorieva and A. A. Firsov, *Science*, 2004, **306**, 666–669.
- Y. Zhang, T. Liu, B. Meng, X. Li, G. Liang, X. Hu and Q. J. Wang, *Nat. Commun.*, 2013, **4**, 1811.
- F. Koppens, T. Mueller, P. Avouris, A. Ferrari, M. Vitiello and M. Polini, *Nat. Nanotechnol.*, 2014, **9**, 780–793.
- Y. Liu, R. Cheng, L. Liao, H. Zhou, J. Bai, G. Liu, L. Liu, Y. Huang and X. Duan, *Nat. Commun.*, 2011, **2**, 579.
- F. H. Koppens, D. E. Chang and F. J. Garcia de Abajo, *Nano Lett.*, 2011, **11**, 3370–3377.
- K. Roy, M. Padmanabhan, S. Goswami, T. P. Sai, G. Ramalingam, S. Raghavan and A. Ghosh, *Nat. Nanotechnol.*, 2013, **8**, 826–830.
- D. Sun, G. Aivazian, A. M. Jones, J. S. Ross, W. Yao, D. Cobden and X. Xu, *Nat. Nanotechnol.*, 2012, **7**, 114–118.
- T. Mueller, F. Xia, M. Freitag, J. Tsang and P. Avouris, *Phys. Rev. B: Condens. Matter*, 2009, **79**, 245430.
- J. Yan, M. H. Kim, J. A. Elle, A. B. Sushkov, G. S. Jenkins, H. M. Milchberg, M. S. Fuhrer and H. Drew, *Nat. Nanotechnol.*, 2012, **7**, 472–478.
- X. An, F. Liu, Y. J. Jung and S. Kar, *Nano Lett.*, 2013, **13**, 909–916.

- 27 S. Tongay, T. Schumann and A. Hebard, *Appl. Phys. Lett.*, 2009, **95**, 222103.
- 28 W. J. Yu, Y. Liu, H. Zhou, A. Yin, Z. Li, Y. Huang and X. Duan, *Nat. Nanotechnol.*, 2013, **8**, 952–958.
- 29 W. Guo, S. Xu, Z. Wu, N. Wang, M. Loy and S. Du, *Small*, 2013, **9**, 3031–3036.
- 30 W. Zhang, C.-P. Chuu, J.-K. Huang, C.-H. Chen, M.-L. Tsai, Y.-H. Chang, C.-T. Liang, Y.-Z. Chen, Y.-L. Chueh, J.-H. He, M.-Y. Chou and L.-J. Li, *Sci. Rep.*, 2014, **4**, 3826.
- 31 H. Qiao, J. Yuan, Z. Xu, C. Chen, S. Lin, Y. Wang, J. Song, Y. Liu, Q. Khan, H. Y. Hoh, C.-X. Pan, S. Li and Q. Bao, *ACS Nano*, 2015, **9**, 1886–1894.
- 32 Z. Sun and H. Chang, *ACS Nano*, 2014, **8**, 4133–4156.
- 33 C.-H. Liu, Y.-C. Chang, T. B. Norris and Z. Zhong, *Nat. Nanotechnol.*, 2014, **9**, 273–278.
- 34 G. Konstantatos, M. Badioli, L. Gaudreau, J. Osmond, M. Bernechea, F. P. G. de Arquer, F. Gatti and F. H. Koppens, *Nat. Nanotechnol.*, 2012, **7**, 363–368.
- 35 D. Tsiulyanu, A. Tsiulyanu, H.-D. Liess and I. Eisele, *Thin Solid Films*, 2005, **485**, 252–256.
- 36 N. Miura and S. Tanaka, *Appl. Phys. Lett.*, 1968, **12**, 374–375.
- 37 T. I. Lee, S. Lee, E. Lee, S. Sohn, Y. Lee, S. Lee, G. Moon, D. Kim, Y. S. Kim, J. M. Myoung and Z. L. Wang, *Adv. Mater.*, 2013, **25**, 2920–2925.
- 38 S. K. Yee, N. E. Coates, A. Majumdar, J. J. Urban and R. A. Segalman, *Phys. Chem. Chem. Phys.*, 2013, **15**, 4024–4032.
- 39 B. Levine, C. Bethea, G. Hasnain, J. Walker and R. Malik, *Appl. Phys. Lett.*, 1988, **53**, 296–298.
- 40 T. Rauch, M. Böberl, S. F. Tedde, J. Fürst, M. V. Kovalenko, G. Hesser, U. Lemmer, W. Heiss and O. Hayden, *Nat. Photonics*, 2009, **3**, 332–336.
- 41 M. Graf, N. Hoyler, M. Giovannini, J. Faist and D. Hofstetter, *Appl. Phys. Lett.*, 2006, **88**, 241118.
- 42 A. Stiff, S. Krishna, P. Bhattacharya and S. Kennerly, *Appl. Phys. Lett.*, 2001, **79**, 421–423.
- 43 X. Hu, Y. Dong, F. Huang, X. Gong and Y. Cao, *J. Phys. Chem. C*, 2013, **117**, 6537–6543.
- 44 B. Torrie, *Solid State Commun.*, 1970, **8**, 1899–1901.
- 45 A. Ferrari, J. Meyer, V. Scardaci, C. Casiraghi, M. Lazzeri, F. Mauri, S. Piscanec, D. Jiang, K. Novoselov, S. Roth and A. Geim, *Phys. Rev. Lett.*, 2006, **97**, 187401.
- 46 K. Roy, M. Padmanabhan, S. Goswami, T. P. Sai, S. Kaushal and A. Ghosh, *Solid State Commun.*, 2013, **175**, 35–42.
- 47 T. Mueller, F. Xia and P. Avouris, *Nat. Photonics*, 2010, **4**, 297–301.
- 48 M. Freitag, T. Low, F. Xia and P. Avouris, *Nat. Photonics*, 2013, **7**, 53–59.
- 49 M. Ataka, R. Yoshizaki and S. Tanaka, *Solid State Commun.*, 1973, **13**, 849–851.
- 50 U. Chandni, P. Kundu, A. K. Singh, N. Ravishankar and A. Ghosh, *ACS Nano*, 2011, **5**, 8398–8403.
- 51 U. Chandni, P. Kundu, S. Kundu, N. Ravishankar and A. Ghosh, *Adv. Mater.*, 2013, **25**, 2486–2491.
- 52 P. Kundu, U. Chandni, A. Ghosh and N. Ravishankar, *Nanoscale*, 2012, **4**, 433–437.
- 53 S. W. Finefrock, H. Fang, H. Yang, H. Darsono and Y. Wu, *Nanoscale*, 2014, **6**, 7872–7876.